

Unmasking short-range correlations via initial-state fluctuations in relativistic heavy-ion collisions

Pei Li,^{1,2} Kai-Jia Sun,^{1,2,*} Bo Zhou,^{1,2,†} and Guo-Liang Ma^{1,2,‡}

¹Key Laboratory of Nuclear Physics and Ion-beam Application (MOE),
Institute of Modern Physics, Fudan University, Shanghai 200433, China

²Shanghai Research Center for Theoretical Nuclear Physics,
NSFC and Fudan University, Shanghai 200438, China

Although relativistic heavy-ion collisions have emerged as a powerful probe for studying nuclear structure, the potential influence of nucleon-nucleon short-range correlations (NN-SRCs) on the initial state has remained an open question. By incorporating NN-SRCs into the initial conditions, we demonstrate that higher-order fluctuations of the initial transverse size, n -particle $c_{E/S}\{n\}$, which can be directly mapped to final-state mean transverse momentum fluctuations, exhibit remarkable sensitivity to NN-SRCs. Quantitatively, $c_{E/S}\{3\}$ and $c_{E/S}\{4\}$ differ by more than 10% between systems with and without NN correlations. Moreover, we report a universal scaling of these quantities with $A^{-1/3}$ and the average nuclear density, mirroring the connection between the SRC effect and the EMC effect in electron scatterings. This work establishes relativistic heavy-ion collisions as a new tool for probing nuclear structure and constraining two-body or many-body NN interactions across different energy scales and system sizes.

I. INTRODUCTION

In relativistic heavy-ion collisions, atomic nuclei collide at nearly the speed of light, transiently forming an extreme state of matter known as the quark-gluon plasma (QGP), a new phase of quantum chromodynamics (QCD) matter at extremely high temperature and density [1–3]. These collisions provide a unique platform to snapshot nuclear structure [4, 5]. The observables of the final state, such as anisotropic flow (v_n) and transverse momentum fluctuations (δp_T), are not only governed by the hydrodynamic evolution of the QGP, but also sensitive to the geometry of the initial state and density fluctuations in the colliding nuclei [6–10]. A precise understanding of final-state observables in heavy-ion collisions relies critically on the initial nucleon distribution for colliding nuclei. This reliance is grounded in the linear hydrodynamic response relations, i.e., $v_n \propto \varepsilon_n$ [11–14] and $\delta p_T \propto \delta d_\perp$ [15–18], where ε_n and d_\perp correspond to the geometry and inverse size of the initial density distribution, respectively. To achieve a more quantitative understanding of the QGP properties, improved initial-state models that incorporate refined nuclear structure effects are imperative.

Although the single nucleon density distribution $\rho^{(1)}(r)$ without NN correlations has successfully described many initial-state properties in relativistic heavy-ion collisions [5, 19–21], it fails to capture the full complexity of nuclear many-body dynamics due to its oversimplified picture. Given that $\rho^{(1)}(r)$ obviously lacks information on NN correlations, capturing the lowest-order correlations requires moving to the two-body den-

sity $\rho^{(2)}(\mathbf{r}_1, \mathbf{r}_2)$ for the initial state. This limitation is underscored by experimental observations of the nucleon momentum distribution, which reveal a significant high-momentum tail (HMT) with approximately 20% of nucleons carrying momenta well above the Fermi momentum ($k_F \approx 250$ MeV/c) [22, 23]. This phenomenon, which cannot be explained by independent nucleon motion in mean fields, is the key experimental evidence for the existence of NN short-range correlations (NN-SRCs) within the nucleus [24–32]. Extensive experimental evidence from a wide range of nuclei, from light to heavy (e.g. ^{12}C , ^{56}Fe and ^{208}Pb), shows that the number of neutron-proton (np) SRC pairs far exceeds that of proton-proton (pp) or neutron-neutron (nn) pairs (about 20 times in ^{12}C) [33]. It strongly supports the dominant role of the tensor force component [34, 35], which is most significant in the np pair channel while being suppressed in the pp/nn pairs due to the inherent Pauli exclusion principle.

The NN-SRCs effect has profound connections with other intriguing phenomena in nuclear physics. A particularly striking finding is that there exists a precise linear relationship between the abundance of SRC pairs and the magnitude of the EMC effect [36–38], whose physical origin has long lacked a universally accepted explanation [24, 36, 39]. In addition, insights provided by NN-SRCs into the short-range nucleon-nucleon interaction are crucial for understanding the Equation of State (EOS) of dense neutron stars [40, 41] and neutrinoless double beta decay ($0\nu\beta\beta$) [42]. In principle, if the SRC-induced localization of nucleon pairs leaves a distinct imprint on the initial QGP energy density, it is then mapped to final-state observables by the subsequent hydrodynamically governed evolution, thus providing a unique opportunity to study nucleon-nucleon correlations.

In the present study, we systematically investigate the influence of NN correlations on initial-state density fluctuations in heavy-ion collisions. Analytical theoretical calculations are performed using a non-spherical tetrahe-

*kjsun@fudan.edu.cn

†zhou_bo@fudan.edu.cn

‡glma@fudan.edu.cn

dral cluster structure to characterize the NN correlation effect of the ^{16}O nucleus, which provides a theoretical benchmark for the sensitivity of NN correlation effect. We utilize the initial-state T_{RENT}o model to examine a series of higher-order quantities in the ultra-central collisions and identify their sensitivity to NN correlations. Furthermore, we compare the performance of NN correlation effect in different sizes of nuclei (e.g. ^{16}O , ^{40}Ca and ^{208}Pb) to reveal the consistency of scaling behavior across system sizes and energy scales. Our results pave the way for future experimental studies to achieve a quantitative isolation of NN correlation effect in relativistic heavy-ion collisions.

II. METHODS FOR NN-CORRELATED DENSITIES

A. Analytical framework

The nuclear structure, including its shape, clustering and size, can be probed via high-energy heavy-ion collisions, based on analytical calculations of the one-body density distribution [17, 18, 43]. A typical one-body nucleon density distribution is obtained by integrating the A -body nucleon density over $A - 1$ dimensions:

$$\rho^{(1)}(\mathbf{r}_1) = A \int |\Phi(\mathbf{r}_1, \mathbf{r}_2, \dots, \mathbf{r}_A)|^2 d\mathbf{r}_2 d\mathbf{r}_3 \dots d\mathbf{r}_A, \quad (1)$$

where $\Phi(\mathbf{r}_1, \mathbf{r}_2, \dots, \mathbf{r}_A)$ is A -body wave function and the square of the wave function $|\Phi|^2$ represents the A -body density distribution. However, the one-body density obviously does not contain the natural NN correlations. The existing correlations in previous studies on nuclear structure in heavy-ion collisions were simply brought about by the Wigner rotation integral [44, 45]. To include the lowest-order NN correlations, the two-body nucleon density can be obtained by integrating over $A - 2$ dimensions [46]:

$$\rho^{(2)}(\mathbf{r}_1, \mathbf{r}_2) = A(A-1) \int |\Phi(\mathbf{r}_1, \mathbf{r}_2, \dots, \mathbf{r}_A)|^2 d\mathbf{r}_3 d\mathbf{r}_4 \dots d\mathbf{r}_A. \quad (2)$$

If we consider the lowest-order two-body NN correlation, then it satisfies

$$\rho^{(2)}(\mathbf{r}_1, \mathbf{r}_2) \neq \rho^{(1)}(\mathbf{r}_1)\rho^{(1)}(\mathbf{r}_2). \quad (3)$$

Similarly, to characterize multi-body correlations, we define them through the density distributions via the relation of $\rho^{(A)}(\mathbf{r}_1, \mathbf{r}_2, \dots, \mathbf{r}_A) \neq \prod_i \rho^{(1)}(\mathbf{r}_i)$. The NN correlations originate from both statistical effects (e.g., Pauli exclusion and antisymmetrization) and dynamical effects due to the nature of the nuclear force. In a precise Hamiltonian, we need to include numerous manybody correlation operators, which leads to very complex calculations. To conveniently represent correlations, two-point correlation functions $F(\mathbf{r}_1, \mathbf{r}_2)$ are typically used to describe

NN correlations [47, 48],

$$F(\mathbf{r}_1, \mathbf{r}_2) = \frac{\rho^{(2)}(\mathbf{r}_1, \mathbf{r}_2)}{\rho^{(1)}(\mathbf{r}_1)\rho^{(1)}(\mathbf{r}_2)}. \quad (4)$$

Evidently, the correlation function depends on the form of the interaction adopted in manybody calculations [49, 50]. We uniformly adopt the parameterized form recommended in Ref. [47],

$$F(\Delta r) = 1 + e^{-\alpha(\Delta r)^2}(\gamma + \prod_i \beta_i(\Delta r)^{i+1}), \quad (5)$$

where $\Delta r = |\mathbf{r}_1 - \mathbf{r}_2|$ denotes the relative distance between the two nucleons. The parameter α is used to control the range of interaction and the parameter γ is used to control the nature of the interaction, as shown in Fig. 1(b). Specifically, $\gamma > 0$ indicates an attractive potential, $\gamma < 0$ signifies a repulsive potential, and $\gamma = 0$ or $\alpha \rightarrow \infty$ means there are no correlations. The resulting nucleon distributions for these cases are illustrated in Fig. 1(a). In expansion terms, β_1 , β_2 , and β_3 are higher-order expansion terms that correspond to medium- and long-range properties.

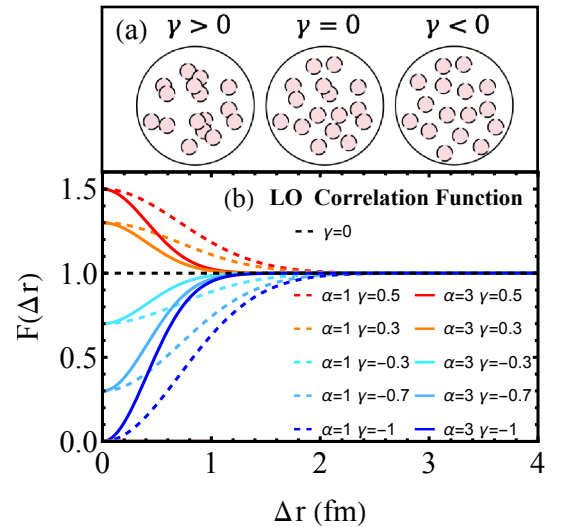


FIG. 1: The schematic nucleon distributions from NN correlations under different γ parameters (a) and the parameterized leading-order two-point correlations (b).

The two-body density distribution and the one-body density distribution are related. Thus, the effective one-body density $\rho_{\text{cor}}^{(1)}(\mathbf{r}_1)$, which incorporates NN correlations, is given by

$$\rho_{\text{cor}}^{(1)}(\mathbf{r}_1) = \frac{1}{A-1} \int \rho^{(2)}(\mathbf{r}_1, \mathbf{r}_2) d\mathbf{r}_2, \quad (6)$$

where $\rho^{(2)}(\mathbf{r}_1, \mathbf{r}_2) = F(\mathbf{r}_1, \mathbf{r}_2)\rho^{(1)}(\mathbf{r}_1)\rho^{(1)}(\mathbf{r}_2)$ according to Eq. (4). To facilitate analytical integral calculations,

we introduced different leading-order correlation functions $F(\Delta r) = 1 + \gamma e^{-\alpha(\Delta r)^2}$, as shown in Fig. 1(b). Building on the framework for ^{20}Ne in Ref. [43], we extend the approach to evaluate expectation values via the effective one-body density, which equivalently performs the two-body integration incorporating the NN correlation function, as shown in the Appendix A. We introduce isospin-independent and isospin-dependent NN correlation functions, as detailed in the Appendices B and C.

Following Ref. [51, 52], we represent ^{16}O in analytical calculations by a frozen cluster structure with the approximate one-body density $\rho^{(1)}(\mathbf{r}) = \sum_i \rho_{\alpha_i}(\mathbf{r}, \mathbf{R}_i)$, where $\rho_{\alpha_i}(\mathbf{r}, \mathbf{R}_i) = (\frac{1}{\pi b^2})^{\frac{3}{2}} \exp[-\frac{1}{b^2}(\mathbf{r} - \mathbf{R}_i)^2]$ is the distribution of the nucleons in the i -th alpha cluster, \mathbf{R}_i is the center-of-mass position of the i -th cluster, and b is the harmonic oscillator size.

B. Adaptive Monte Carlo sampling

We expect to investigate the NN correlation effect while maintaining identical one-body density distribution, thus avoiding interference from mean field effects. Sampling is performed using the following formula:

$$\rho_{cor}^{(A)}(\mathbf{r}_1, \mathbf{r}_2, \dots, \mathbf{r}_A) = |\Phi(\mathbf{r}_1, \mathbf{r}_2, \dots, \mathbf{r}_A)|^2 \prod_{i \neq j} F(\mathbf{r}_i, \mathbf{r}_j), \quad (7)$$

where $|\Phi(\mathbf{r}_1, \mathbf{r}_2, \dots, \mathbf{r}_A)|^2$ satisfies exchange antisymmetry and includes the statistical correlations caused by the Pauli exclusion principle, and $\prod_{i \neq j} F(\mathbf{r}_i, \mathbf{r}_j)$ includes the dynamical correlations arising from the nature of the NN interactions. Specifically, for nuclei with a Woods-Saxon (WS) distribution $\rho(r) = \rho_0(1 + wr^2/R_0^2)/(1 + \exp[(r - R_0)/a])$, the following formula is employed for sampling:

$$\rho_{WS,cor}^{(A)}(\mathbf{r}_1, \mathbf{r}_2, \dots, \mathbf{r}_A) = \prod_i \rho_{WS}^{(1)}(\mathbf{r}_i) \prod_{i \neq j} F(\mathbf{r}_i, \mathbf{r}_j). \quad (8)$$

It has been a challenging task to accurately sample the multidimensional spatial distributions given in Eqs. (7) and (8) in high-energy nuclear physics research [48, 53, 54]. The widely used Markov Chain Monte Carlo (MCMC) sampling [48, 55] becomes inefficient in high dimensions. To address this issue, in the present study, we utilize an improved importance sampling method based on the VEGAS method [56, 57] for high-dimensional integration. To estimate the multidimensional integral $I = \int f(x)dx$, the Vegas algorithm maps the uniform grid in y space to a curved grid in x space for each dimension. This is achieved by minimizing the variance of the estimate σ_I^2 ,

$$\sigma_I^2 = \frac{1}{N_{ev}} \left[\int_0^1 dy [J(y, x)f(x(y))]^2 - I^2 \right], \quad (9)$$

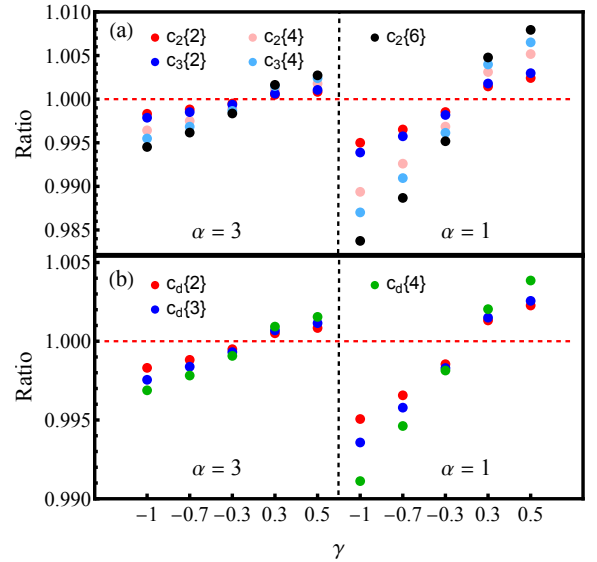


FIG. 2: The analytical results for ratios of initial-state cumulants in ultracentral $^{16}\text{O}+^{16}\text{O}$ collisions: (a) eccentricity cumulants and (b) inverse transverse size cumulants.

where N_{ev} is the number of sampling points in each iteration, $J(y, x)$ is the Jacobian of the coordinate transformation.

For a perfect mapping, the Jacobian J is proportional to the inverse of the integrand, i.e., $J \propto f^{-1}$, and $\sigma_I^2 = 0$. In this case, one can make a uniform sampling in y space and then map it into x space, and the distribution of samples in x space now follows exactly the form of $f(x)$. The adaptive method in Vegas is far faster and more efficient than MCMC in high dimensions. However, the mapping is generally imperfect, particularly for distributions that cannot be factorized in high dimensions. To improve sampling, we first generate events using the VEGAS algorithm and then apply an accept-reject procedure to enforce the target distribution. We have verified that the resulting samples accurately encode the NN correlations.

III. RESULTS AND DISCUSSION

In analytical calculations, only non-spherical nuclear structures have non-zero eccentricities and inverse transverse size fluctuations because of the neglect of nucleon position fluctuations [43]. We choose an unconventional tetrahedral 4α -cluster structure ($D_1 = 1.6$ fm, $D_2 = 3.5$ fm) to characterize the one-body density for our analytical calculations. This structure theoretically possesses large ε_2 and ε_3 , which allows it to manifest changes more significantly resulting from NN correlation effect alone. The details can be found in the Appendix D. By setting $b = 1.76$ fm, the resulting root-mean-square (RMS) radius of ^{16}O , $\sqrt{\langle r^2 \rangle} = 2.7$ fm is consistent with the ex-

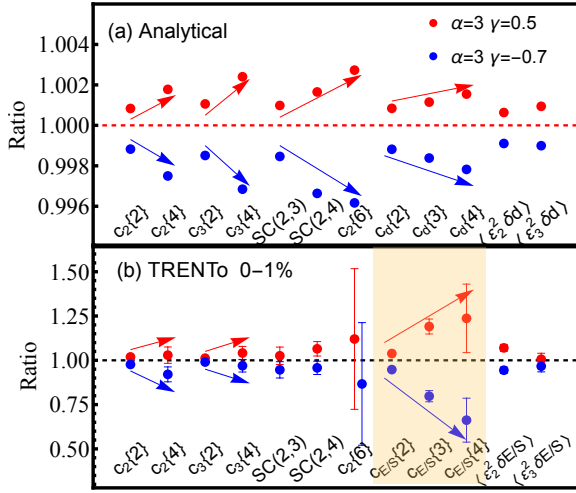


FIG. 3: Ratios $R(Q) = Q_{\text{cor}}/Q_{\text{uncor}}$ for various observables Q in ultracentral $^{16}\text{O}+^{16}\text{O}$ collisions under attractive (red) and repulsive (blue) leading-order NN correlations: (a) Analytical results for a tetrahedral 4α -cluster structure, and (b) TReNTo results using a Woods-Saxon (WS) distribution.

perimental charge RMS radius 2.73 fm.

Figure 2 shows the ratio $R(Q) = Q_{\text{cor}}/Q_{\text{uncor}}$, which quantifies the relative change induced by NN correlations for quantity Q . When $\gamma > 0$, the attractive effect causes a slight increase in the various quantities, whereas the repulsive effect causes a slight decrease when $\gamma < 0$. To identify the most sensitive quantities, we compute all initial-state quantities for two cases with $\alpha = 3$ in Fig. 3(a). While rooted in a two-point correlation function, higher-order multiparticle quantities display a strikingly enhanced sensitivity to NN correlations over their two-particle counterparts. We quantify the relative sensitivity via $\Delta R(Q) = |R(Q) - 1|$, which leads to the two observed hierarchies:

$$\Delta R(c_n\{6\}) > \Delta R(c_n\{4\}) > \Delta R(c_n\{2\}), \quad (10)$$

$$\Delta R(c_d\{4\}) > \Delta R(c_d\{3\}) > \Delta R(c_d\{2\}). \quad (11)$$

To investigate the impact of NN correlations in the presence of nucleon position fluctuations, we employ the initial geometry model TReNTo to simulate the initial state of heavy-ion collisions. The inelastic nucleon-nucleon cross section and nucleon width are set to $\sigma_{NN} = 70.9$ mb and $w = 0.4$ fm, respectively, for LHC energy $\sqrt{s_{NN}} = 5.36$ TeV, with the centrality defined by the initial entropy density S . In the TReNTo model, the number of charged particles is given by $N_{ch} = \int dx dy [(T_A^p + T_B^p)/2]^{1/p}$, where $p = 0$ is used in this work. The remaining parameters are consistent with those in Ref. [58]. A spherical Woods-Saxon distribution is used for ^{16}O , with parameters provided in Table I

along with those of the other two nuclei. The system size is characterized by E/S rather than d_\perp , due to its more direct physical relevance to the initial energy density [59].

Figure 3(b) shows the corresponding TReNTo results for 0–1% centrality under attractive ($\gamma = 0.5$) and repulsive ($\gamma = -0.7$) leading-order correlations. The NN correlation effect revealed by the TReNTo results agrees with the analytical trend and follows the hierarchies given in Eqs. (10) and (11). However, higher-order quantities such as $c_2\{6\}$ suffer from nucleon position fluctuations, which make the two cases indistinguishable within the present statistical precision. The inclusion of nucleon-position fluctuations in the TReNTo model enhances the NN correlation effect, making it more prominent than that in analytical calculations, as it directly amplifies fluctuations in the initial-state energy density. However, the effect of NN correlations on eccentricity ϵ_n is very limited, as reflected in different three-point correlation quantities, and we find that

$$\Delta R(c_{E/S}\{3\}) > \Delta R(\langle \epsilon_2^2 \delta(E/S) \rangle) \approx \Delta R(\langle \epsilon_3^2 \delta(E/S) \rangle). \quad (12)$$

For the 3- and 4-point correlators $c_{E/S}\{n\}$, a relative deviation $\Delta R(c_{E/S}\{n\}) \approx 20\%$ remains statistically significant despite nucleon fluctuations in the WS distribution, which can be verified using the distribution of $\langle E/S \rangle$ in the Appendix E. Therefore, final-state transverse momentum correlations $\langle (\delta p_T)^n \rangle$ ($n > 2$) emerge as promising candidates to probe NN correlations with enhanced sensitivity. This indicates that the properties of NN correlations are an essential input for a complete theoretical description of higher-order final-state transverse momentum fluctuations, including skewness [62] and kurtosis.

Using the two-point correlation function fitted with the Alvioli-AV8' interaction from Ref. [48], we investigate NN correlations in three nearly spherical nuclear collision systems of different sizes. For the nuclei ^{16}O , ^{40}Ca , and ^{208}Pb , the WS distributions are used with the parameters in Table I. The deuterium ^2H serves as the NN correlations baseline and is modeled by two localized nucleon wave functions. The top and bottom panels of Fig. 4 display the dependence of $\Delta R(c_{E/S}\{n\})$ on $A^{-1/3}$ and the average nuclear density, respectively, where the latter is calculated assuming a uniform sphere with a radius matching the RMS charge radius. The NN correlation effect becomes more pronounced in larger systems owing to the increased nucleon density and suppressed position fluctuations, which collectively make the correlation sig-

TABLE I: WS distribution parameters used for the TReNTo model in spherically structured from Refs. [60, 61] and the number of nucleons per unit volume.

nucleus	R_0 (fm)	w	a (fm)	r_{RMS} (fm)	$\bar{\rho}$ (fm $^{-3}$)
^{16}O	2.608	-0.511	0.513	2.73	0.087
^{40}Ca	3.766	-0.161	0.586	3.48	0.094
^{208}Pb	6.49	-	0.54	5.5	0.125

nal more visible.

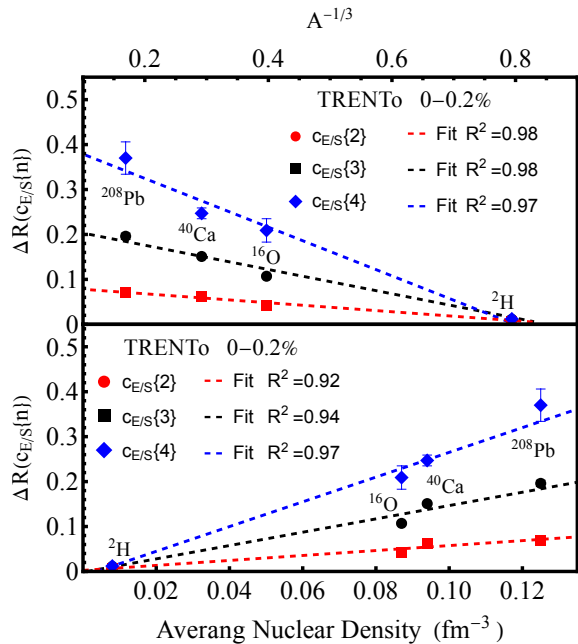


FIG. 4: The dependence of $\Delta R(c_{E/S}\{n\})$ on $A^{-1/3}$ (top panel) and the average nuclear density (bottom panel) with AV8' interaction in ^{16}O , ^{40}Ca and ^{208}Pb . The coefficient of determination R^2 denotes the quality of the linear fitting.

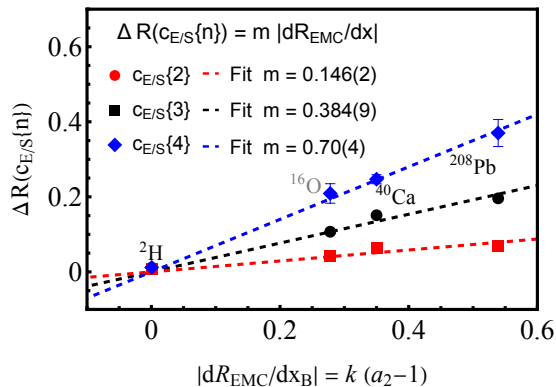


FIG. 5: The linear dependence of $\Delta R(c_{E/S}\{n\})$ on the EMC effect $|dR_{EMC}/dx_B|$. The EMC results of ^{40}Ca and ^{208}Pb represents the data from SLAC and Jefferson Lab [38, 63, 64], and the results of ^{16}O are from Effective Field Theory [65]. The linear scaling coefficient k of the EMC-SRC relationship is approximately 0.08.

A similar dependence on $A^{-1/3}$ and the average nucleon number density has also been found in studies of the SRC effect [66, 67] and the EMC effect [64, 68]. The magnitude of the EMC effect is quantified by the slope $|dR_{EMC}/dx_B| = k(a_2 - 1)$ obtained from a linear fit to $R_{EMC} = (F_2^A/A)/(F_2^D/2)$ in DIS experiments with the intermediate Bjorken region $0.3 < x_B < 0.7$, where a_2 denotes the relative probability of finding an SRC pair in

the nucleus A compared to finding one in the deuteron within the range $1.3 < x_B < 2$, reflecting the magnitude of the SRC effect [29, 64, 69]. Fig. 5 exhibits a linear dependence of $\Delta R(c_{E/S}\{n\})$ on $|dR_{EMC}/dx_B|$, mirroring the phenomenological EMC-SRC correlation seen in the studies of low-energy electron scattering [37, 70] and pointing to a shared physical origin based on high local density. Our findings bridge medium modifications in heavy-ion collisions and deep-inelastic scattering: although the relevant Bjorken x_B differs by two orders of magnitude ($x_B \approx \frac{m_T}{\sqrt{s_{NN}}}e^{\pm y} \sim 0.01$ in HICs [71] vs. $x_B > 0.3$ in electron scattering experiments), both phenomena appear driven by a unified origin—NN correlations imprinted in both hot and cold QCD matter.

IV. CONCLUSION AND OUTLOOK

Using an analytical method to theoretically incorporate NN correlations, we predict the respective influences of attractive and repulsive potentials on initial-state quantities. Through an improved Monte Carlo sampling method, which precisely obtains initial-state nuclear samples with NN correlations, we validate the results of our theoretical analysis using the TRENTTo model. This work identifies higher-order fluctuations in the transverse size $c_{E/S}\{n\}$ as highly sensitive quantities to NN correlations. Quantitative results show that the relative deviation of $c_{E/S}\{3\}$ and $c_{E/S}\{4\}$ can exceed 10% between systems with and without NN correlations in ultra-central collisions. Furthermore, we first discover the linear scaling property of the NN-SRCs effect in heavy-ion collisions, which is surprisingly consistent with findings in previous EMC and SRC studies in low-energy experiments. By definitively establishing a robust linear correlation between the $\Delta R(c_{E/S}\{n\})$ and the EMC effect, this work builds a phenomenological bridge linking the short range structure of cold nuclear matter driven by NN correlations and high local density fluctuations in the initial state dynamics of relativistic heavy-ion collisions. This finding provides new constraints for theoretical models of the event-by-event initial geometry in the heavy-ion experiments LHC and RHIC, thus advancing our fundamental understanding of the properties of dense nuclear matter.

The current study only considers the NN correlation within a fixed structural space. In the future, it can be extended to a mixed basis based on the GCM model [72] to study the shape mixing of clusters, and nuclear deformation, such as deformed nuclei ^{238}U with β_2 and β_3 deformations [5] and ^{208}Pb with β_3 deformation fluctuations [73], to systematically explore the complex interplay between cluster structure, deformation and NN correlation effect.

Acknowledgment

Discussions with Shu-jie Li, Nir Barnea, Bai Dong, Hao-yu Shang, Niu Wan, Bao-jun Cai, and Chun-jian Zhang are gratefully acknowledged. This work is supported by the National Natural Science Foundation of China under Grants No. 12325507, No. 12147101, and

No. 123B1011, No. 12422509, No. 12375121, the National Key Research and Development Program of China under Grant No. 2022YFA1604900, 2024YFA1612500, and the Guangdong Major Project of Basic and Applied Basic Research under Grant No. 2020B0301030008. The computations in this research were performed using the CFFF platform of Fudan University.

-
- [1] K. Adcox et al. (PHENIX), Nucl. Phys. A **757**, 184 (2005), nucl-ex/0410003.
 - [2] J. Adams et al. (STAR), Nucl. Phys. A **757**, 102 (2005), nucl-ex/0501009.
 - [3] K. Aamodt et al. (ALICE), Phys. Rev. Lett. **105**, 252302 (2010), 1011.3914.
 - [4] S. Acharya et al. (ALICE), Phys. Lett. B **784**, 82 (2018), 1805.01832.
 - [5] M. I. Abdulhamid et al. (STAR), Nat. **635**, 67 (2024), 2401.06625.
 - [6] J.-Y. Ollitrault, Phys. Rev. D **46**, 229 (1992).
 - [7] U. Heinz and R. Snellings, Ann. Rev. Nucl. Part. Sci. **63**, 123 (2013), 1301.2826.
 - [8] C. Joslin and C. Gray, Molecular Physics **50**, 329 (1983).
 - [9] D. Teaney and L. Yan, Phys. Rev. C **83**, 064904 (2011).
 - [10] C. Zhang, J. Chen, G. Giacalone, S. Huang, J. Jia, and Y.-G. Ma, Phys. Lett. B **862**, 139322 (2025), 2404.08385.
 - [11] B. Alver and G. Roland, Phys. Rev. C **81**, 054905 (2010), 1003.0194.
 - [12] H. Niemi, K. J. Eskola, and R. Paatelainen, Phys. Rev. C **93**, 024907 (2016).
 - [13] D. Teaney and L. Yan, Phys. Rev. C **86**, 044908 (2012).
 - [14] G. Nijs, W. van der Schee, U. Gürsoy, and R. Snellings, Phys. Rev. Lett. **126**, 202301 (2021), 2010.15130.
 - [15] A. Bilandzic, R. Snellings, and S. Voloshin, Phys. Rev. C **83**, 044913 (2011), 1010.0233.
 - [16] A. Bilandzic, C. H. Christensen, K. Gulbrandsen, A. Hansen, and Y. Zhou, Phys. Rev. C **89**, 064904 (2014), 1312.3572.
 - [17] J. Jia, Phys. Rev. C **105**, 014905 (2022), 2106.08768.
 - [18] J. Jia, Phys. Rev. C **105**, 044905 (2022), 2109.00604.
 - [19] C. Zhang and J. Jia, Phys. Rev. Lett. **128**, 022301 (2022), 2109.01631.
 - [20] S. Acharya et al. (ALICE), Phys. Lett. B **834**, 137393 (2022), 2111.06106.
 - [21] S. Zhao, H.-j. Xu, Y. Zhou, Y.-X. Liu, and H. Song, Phys. Rev. Lett. **133**, 192301 (2024), 2403.07441.
 - [22] O. Benhar, A. Fabrocini, and S. Fantoni, Nucl. Phys. A **505**, 267 (1989).
 - [23] A. Polls, A. Ramos, J. Ventura, S. Amari, and W. H. Dickhoff, Phys. Rev. C **49**, 3050 (1994).
 - [24] O. Hen, G. A. Miller, E. Piasetzky, and L. B. Weinstein, Rev. Mod. Phys. **89**, 045002 (2017), 1611.09748.
 - [25] L. L. Frankfurt and M. I. Strikman, Phys. Rept. **160**, 235 (1988).
 - [26] C. Ciofi Degli Atti and S. Liuti, Phys. Lett. B **225**, 215 (1989).
 - [27] J. Arrington, D. W. Higinbotham, G. Rosner, and M. Sargsian, Prog. Part. Nucl. Phys. **67**, 898 (2012), 1104.1196.
 - [28] Z. Ye and J. Arrington, in *13th Conference on the Intersections of Particle and Nuclear Physics* (2018), 1810.03667.
 - [29] Z. Ye, Ph.D. thesis, Physics - Graduate School of Arts and Sciences, University of Virginia (2013), 1408.5861.
 - [30] R. Cruz-Torres, D. Lonardonì, R. Weiss, N. Barnea, D. W. Higinbotham, E. Piasetzky, A. Schmidt, L. B. Weinstein, R. B. Wiringa, and O. Hen, Nature Phys. **17**, 306 (2021), 1907.03658.
 - [31] G.-F. Wei, Q.-J. Zhi, Z.-W. Long, and Z.-W. Long, Nucl. Sci. Tech. **31**, 71 (2020), 1901.10391.
 - [32] L. Shen, B.-S. Huang, and Y.-G. Ma, Phys. Rev. C **105**, 014603 (2022), 2112.10348.
 - [33] R. Subedi et al., Science **320**, 1476 (2008), 0908.1514.
 - [34] M. M. Sargsian, T. V. Abrahamyan, M. I. Strikman, and L. L. Frankfurt, Phys. Rev. C **71**, 044615 (2005), nucl-th/0501018.
 - [35] R. Schiavilla, R. B. Wiringa, S. C. Pieper, and J. Carlson, Phys. Rev. Lett. **98**, 132501 (2007), nucl-th/0611037.
 - [36] O. Hen, E. Piasetzky, and L. B. Weinstein, Phys. Rev. C **85**, 047301 (2012), 1202.3452.
 - [37] L. B. Weinstein, E. Piasetzky, D. W. Higinbotham, J. Gomez, O. Hen, and R. Shneur, Phys. Rev. Lett. **106**, 052301 (2011), 1009.5666.
 - [38] B. Schmookler et al. (CLAS), Nature **566**, 354 (2019), 2004.12065.
 - [39] J. Seely et al., Phys. Rev. Lett. **103**, 202301 (2009), 0904.4448.
 - [40] O. Hen, B.-A. Li, W.-J. Guo, L. B. Weinstein, and E. Piasetzky, Phys. Rev. C **91**, 025803 (2015), 1408.0772.
 - [41] B.-A. Li, B.-J. Cai, L.-W. Chen, and J. Xu, Prog. Part. Nucl. Phys. **99**, 29 (2018), 1801.01213.
 - [42] J. Menendez, A. Poves, E. Caurier, and F. Nowacki, J. Phys. Conf. Ser. **312**, 072005 (2011).
 - [43] P. Li, B. Zhou, and G.-L. Ma (2025), 2504.04688.
 - [44] G. Giacalone, Eur. Phys. J. A **59**, 297 (2023), 2305.19843.
 - [45] H. Mehrabpour (2025), 2506.12673.
 - [46] Y. Kanada-En'yo, H. Feldmeier, and T. Suhara, Phys. Rev. C **84**, 054301 (2011), 1107.5616.
 - [47] R. Cruz-Torres, A. Schmidt, G. A. Miller, L. B. Weinstein, N. Barnea, R. Weiss, E. Piasetzky, and O. Hen, Phys. Lett. B **785**, 304 (2018), 1710.07966.
 - [48] M. Alvioli, H. J. Drescher, and M. Strikman, Phys. Lett. B **680**, 225 (2009), 0905.2670.
 - [49] I. Korover et al. (CLAS), Phys. Lett. B **820**, 136523 (2021), 2004.07304.
 - [50] A. Schmidt et al. (CLAS), Nature **578**, 540 (2020), 2004.11221.
 - [51] P. Bożek, W. Broniowski, M. Rybczynski, and G. Stefanek, Comput. Phys. Commun. **245**, 106850 (2019), 1901.04484.
 - [52] Y. Wang, S. Zhao, B. Cao, H.-j. Xu, and H. Song, Phys. Rev. C **109**, L051904 (2024), 2401.15723.
 - [53] Y.-J. Huang, Z. Meng, L.-G. Pang, and X.-N. Wang

- (2025), 2504.00790.
- [54] B. P. Kersevan and E. Richter-Was, *Comput. Phys. Commun.* **184**, 919 (2013), hep-ph/0405247.
 - [55] W. K. Hastings, *Biometrika* **57**, 97 (1970).
 - [56] G. P. Lepage, *J. Comput. Phys.* **27**, 192 (1978).
 - [57] G. P. Lepage, *J. Comput. Phys.* **439**, 110386 (2021), 2009.05112.
 - [58] J.-Y. Hu, H.-j. Xu, X. Wang, and S. Pu (2025), 2507.01493.
 - [59] G. Giacalone, F. G. Gardim, J. Noronha-Hostler, and J.-Y. Ollitrault, *Phys. Rev. C* **103**, 024909 (2021), 2004.01765.
 - [60] H. De Vries, C. W. De Jager, and C. De Vries, *Atom. Data Nucl. Data Tabl.* **36**, 495 (1987).
 - [61] M. Rybczynski, G. Stefanek, W. Broniowski, and P. Bozek, *Comput. Phys. Commun.* **185**, 1759 (2014), 1310.5475.
 - [62] G. Giacalone, F. G. Gardim, J. Noronha-Hostler, and J.-Y. Ollitrault, *Phys. Rev. C* **103**, 024910 (2021), 2004.09799.
 - [63] J. Gomez et al., *Phys. Rev. D* **49**, 4348 (1994).
 - [64] J. Arrington, A. Daniel, D. Day, N. Fomin, D. Gaskell, and P. Solvignon, *Phys. Rev. C* **86**, 065204 (2012), 1206.6343.
 - [65] J. E. Lynn, D. Lonardoni, J. Carlson, J. W. Chen, W. Detmold, S. Gandolfi, and A. Schwenk, *J. Phys. G* **47**, 045109 (2020), 1903.12587.
 - [66] T. Liang, D. Bai, and Z. Ren, *Phys. Lett. B* **863**, 139351 (2025), 2410.10202.
 - [67] R. Yankovich, E. Pazy, and N. Barnea, *Phys. Rev. C* **111**, L051304 (2025), 2407.15068.
 - [68] I. Sick and D. Day, *Phys. Lett. B* **274**, 16 (1992).
 - [69] H. Shang, J. Chen, R. Hu, X. Zhen, C. Jiang, and J. Pei, *Phys. Lett. B* **871**, 139976 (2025), 2503.17119.
 - [70] J.-W. Chen, W. Detmold, J. E. Lynn, and A. Schwenk, *Phys. Rev. Lett.* **119**, 262502 (2017), 1607.03065.
 - [71] Ş. Özönder and R. J. Fries, *Phys. Rev. C* **89**, 034902 (2014), 1311.3390.
 - [72] B. Zhou, Y. Funaki, H. Horiuchi, and A. Tohsaki, *Front. Phys.* **15**, 14401 (2020), 1905.00788.
 - [73] H.-j. Xu, D. Xu, S. Zhao, W. Zhao, H. Song, and F. Wang (2025), 2504.19644.
 - [74] J. S. Moreland, J. E. Bernhard, and S. A. Bass, *Phys. Rev. C* **92**, 011901 (2015), 1412.4708.
 - [75] G. Giacalone, Ph.D. thesis, U. Paris-Saclay (2020), 2101.00168.
 - [76] R. S. Bhalerao and J.-Y. Ollitrault, *Phys. Lett. B* **641**, 260 (2006), nucl-th/0607009.
 - [77] S. A. Voloshin, A. M. Poskanzer, A. Tang, and G. Wang, *Phys. Lett. B* **659**, 537 (2008), 0708.0800.
 - [78] E. G. D. Nielsen, F. K. Rømer, K. Gulbrandsen, and Y. Zhou, *Eur. Phys. J. A* **60**, 38 (2024), 2312.00492.
 - [79] P. Bozek, *Phys. Rev. C* **93**, 044908 (2016), 1601.04513.
 - [80] G. A. Miller and J. E. Spencer, *Annals Phys.* **100**, 562 (1976).
 - [81] F. Simkovic, A. Faessler, H. Muther, V. Rodin, and M. Stauf, *Phys. Rev. C* **79**, 055501 (2009), 0902.0331.
 - [82] B. S. Pudliner, V. R. Pandharipande, J. Carlson, S. C. Pieper, and R. B. Wiringa, *Phys. Rev. C* **56**, 1720 (1997), nucl-th/9705009.
 - [83] R. B. Wiringa, V. G. J. Stoks, and R. Schiavilla, *Phys. Rev. C* **51**, 38 (1995), nucl-th/9408016.
 - [84] O. Benhar, R. Biondi, and E. Speranza, *Phys. Rev. C* **90**, 065504 (2014), 1401.2030.
 - [85] R. Machleidt, F. Sammarruca, and Y. Song, *Phys. Rev. C* **53**, R1483 (1996), nucl-th/9510023.

APPENDIX

Appendix A: Initial state quantities

Using the one-body density $\rho^{(1)}$ (with or without NN correlations), the total initial nucleon density in the 2D transverse plane in ultra-central HICs is defined as the arithmetic average of the projectile and target densities,

$$\rho(r_\perp, \phi) = \int [\mathcal{R}_p \rho^{(1)}(\mathbf{r}_1) + \mathcal{R}_t \rho^{(1)}(\mathbf{r}_2)]/2 \, dz, \quad (\text{A1})$$

where \mathcal{R}_p and \mathcal{R}_t are the Euler rotation matrices for the projectile and target nuclei, respectively. The initial-state quantity \mathcal{Q} can be expressed as

$$\begin{aligned} \mathcal{Q} = \langle q(r_\perp) \rangle &= \int q(r_\perp) \rho(r_\perp, \phi) dr_\perp d\Omega_p d\Omega_t \\ &= \int \mathcal{R}_{p,t}(I_p + I_t)/2 \, d\Omega_{p,t}, \end{aligned} \quad (\text{A2})$$

where

$$\begin{aligned} I_{p,t} &= \int q(r_\perp) \rho_{cor}^{(1)}(\mathbf{r}) d\mathbf{r} \\ &= \frac{1}{A-1} \int_{\mathbf{r}_1 \neq \mathbf{r}_2} q(r_\perp) \rho^{(2)}(\mathbf{r}_1, \mathbf{r}_2) d\mathbf{r}_1 d\mathbf{r}_2 \\ &= \frac{1}{A-1} \int_{\mathbf{r}_1 \neq \mathbf{r}_2} q(r_\perp) [1 - C(\mathbf{r}_1, \mathbf{r}_2)] \rho^{(1)}(\mathbf{r}_1) \rho^{(1)}(\mathbf{r}_2) d\mathbf{r}_1 d\mathbf{r}_2 \\ &= \mathcal{Q}_{p,t}^{(1)} - \mathcal{Q}_{p,t}^{(2)}. \end{aligned} \quad (\text{A3})$$

With the relationship $F(\mathbf{r}_1, \mathbf{r}_2) = 1 - C(\mathbf{r}_1, \mathbf{r}_2)$, we divide the expected value into two parts, the one directly generated by the original one-body distribution $\mathcal{Q}_{p,t}^{(1)}$ and the other produced by the two-body correlation distribution $\mathcal{Q}_{p,t}^{(2)}$:

$$\mathcal{Q}_{p,t}^{(1)} = \int q(r_\perp) \rho^{(1)}(\mathbf{r}_1) d\mathbf{r}_1, \quad (\text{A4})$$

$$\mathcal{Q}_{p,t}^{(2)} = \frac{1}{A-1} \int_{\mathbf{r}_1 \neq \mathbf{r}_2} q(r_\perp) C(\mathbf{r}_1, \mathbf{r}_2) \rho^{(1)}(\mathbf{r}_1) \rho^{(1)}(\mathbf{r}_2) d\mathbf{r}_1 d\mathbf{r}_2, \quad (\text{A5})$$

where the $\mathcal{Q}_{p,t}^{(2)}$ contribution is subdominant, $\mathcal{Q}_{p,t}^{(2)} < \mathcal{Q}_{p,t}^{(1)}$. The eccentricity ε_n in the center-of-mass frame is typically used to describe the initial geometrical condition of collisions via 2D multi-pole expansion. The eccentricity vectors are defined as [8, 9, 74],

$$\varepsilon_n e^{in\Phi} = -\frac{\langle r_\perp^n e^{in\phi} \rangle}{\langle r_\perp^n \rangle}, \quad n \geq 2. \quad (\text{A6})$$

Additionally, the size of the initial state can be quantified by the inverse transverse size [43],

$$d_\perp = (\langle x^2 y^2 \rangle - \langle xy \rangle^2)^{-1/4}. \quad (\text{A7})$$

It is worth noting that different models may vary in their definition of the inverse transverse size. As an initial-state output for hydrodynamic models, the TRENTo model typically uses E/S as the initial-state counterpart for transverse momentum [59, 75]. The total energy E and the initial entropy S are defined by $E(\tau_0) = \tau_0 \int \epsilon(\mathbf{x}, \tau_0)$ and $S(\tau_0) = \tau_0 \int s(\mathbf{x}, \tau_0)$, where $\epsilon(\mathbf{x}, \tau_0)$ is the energy density and $s(\mathbf{x}, \tau_0)$ is the entropy density.

With the definitions of nuclear shape and size, we can perform a more refined quantification of high-order fluctuations, e.g. the expressions for eccentricity cumulants [76, 77] of any order:

$$c_n\{2\} = \langle \varepsilon_n^2 \rangle, \quad (\text{A8})$$

$$c_n\{4\} = \langle \varepsilon_n^4 \rangle - 2\langle \varepsilon_n^2 \rangle^2, \quad (\text{A9})$$

$$c_n\{6\} = (\langle \varepsilon_n^6 \rangle - 9\langle \varepsilon_n^4 \rangle \langle \varepsilon_n^2 \rangle + 12\langle \varepsilon_n^2 \rangle^3)/4, \quad (\text{A10})$$

and the expressions for the inverse transverse size cumulants [18, 78] of any order:

$$c_d\{2\} = \langle (\frac{\delta d_\perp}{d_\perp})^2 \rangle, \quad (\text{A11})$$

$$c_d\{3\} = \langle (\frac{\delta d_\perp}{d_\perp})^3 \rangle, \quad (\text{A12})$$

$$c_d\{4\} = \langle (\frac{\delta d_\perp}{d_\perp})^4 \rangle - 3\langle (\frac{\delta d_\perp}{d_\perp})^2 \rangle^2. \quad (\text{A13})$$

In addition, we also consider mixed cumulants, including symmetric cumulants [15, 16],

$$SC(m, n) = \langle \varepsilon_m^2 \varepsilon_n^2 \rangle - \langle \varepsilon_m^2 \rangle \langle \varepsilon_n^2 \rangle, \quad (\text{A14})$$

and the covariance correlation coefficient [79]:

$$\text{cov}(\varepsilon_n^2, \delta d_\perp) = \langle \varepsilon_n^2 \delta d_\perp \rangle. \quad (\text{A15})$$

Regarding the definition of the inverse transverse size cumulants mentioned above, we can similarly use E/S to define the same quantities based on the relationship $E/S \propto d_\perp$, without going into further details here. Based on all of the higher-order correlation quantities discussed above, we explore the sensitive quantities to NN correlations inside atomic nuclei.

Appendix B: NN correlations from different interaction models

Typical two-point correlation functions exhibit a short-range repulsive core at 0-1 fm and a weak attractive

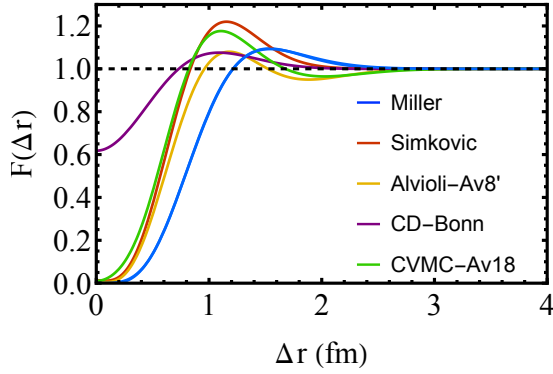


FIG. 6: The two-point correlation function from different interaction models. The results from Miller and Spencer [80], Simkovic [81], Alvioli-AV8' [48, 82], CVMC-AV18 [47, 83], CD-Bonn [84, 85] models are shown for comparison.

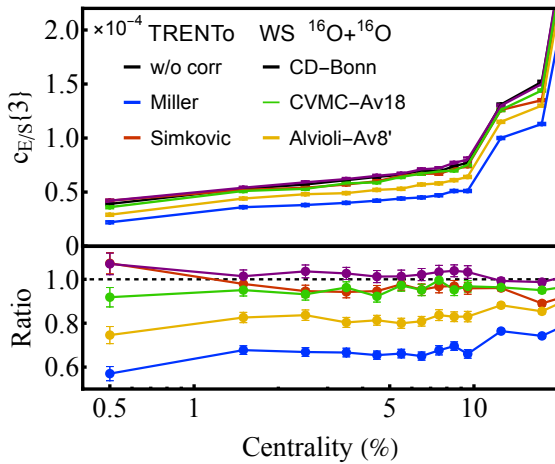


FIG. 7: The TRENTo results on $c_{E/S}\{3\}$ and its ratio $R(c_{E/S}\{3\})$ with different interactions as shown in Fig. 6.

effect around 1 fm, as shown in Fig. 6. The results from different interaction models, including Miller and Spencer [80], Simkovic [81], Alvioli-AV8' [48, 82], CVMC-AV18 [47, 83], CD-Bonn [84, 85], are shown for comparison. We perform a parameter fitting on the two-point correlation functions corresponding to different interactions. The resulting fitting parameters without isospin dependence are presented in Table II, except that the two-point correlation function for CVMC-AV18 is isospin-dependent, and the fitting parameters can be found in Ref [47]. The CD-Bonn interaction has a relatively soft repulsive core, resulting in a weaker repulsive effect ($F(0) \approx 0.6$) and the attractive part of the Simkovic interaction is stronger ($F(1) \approx 1.22$) primarily driven by the tensor force. Consequently, in Fig. 7, the ratio of $c_{E/S}\{3\}$ in ultra-central collisions with CD-Bonn and Simkovic is slightly greater than the results of CVMC-AV18, with the average effect being biased towards attraction. In the Alvioli-AV8' interaction, the at-

TABLE II: Correlation function parameters for different interactions.

Parameters	Miller	Simkovic	Alvioli-AV8'	CD-Bonn
α	1.3977	1.9319	1.2627	1.2746
γ	-0.9965	-0.9868	-0.9816	-0.3820
β_1	1.8195	2.5145	2.1032	-0.8557
β_2	-1.6541	-4.7581	-6.1297	0.1328
β_3	-0.3312	0.0555	2.9348	0.0849

tractive part is weaker ($F(1.2) \approx 1.07$), while the Miller interaction has a longer repulsive range ($F(1.2) \approx 0$). The average correlation effect of these interactions is a very strong repulsive effect. Minute changes in the correlation function caused by different interactions can be reflected in the quantities with higher-order correlations. The relative difference in $c_{E/S}\{3\}$ exhibited by different interactions can reach 40%. This suggests that the NN correlation effect in heavy-ion collisions is potentially a powerful probe for testing interaction models.

Appendix C: NN correlations with isospin dependence

Theoretically, the two-point correlation function is predicted to exhibit a strong isospin dependence that the attractive part of the correlation function in np pairs is stronger than that in pp/nn pairs, while the repulsive part is weaker due to the lack of the Pauli exclusion principle. We employ an adaptive Monte Carlo method to generate isospin-dependent correlated samples. In Fig. 8, pp/nn pairs and np pairs are sampled using distinct correlation functions, represented by the red and blue dashed lines, respectively. We also implement a phenomenological approach that decomposes the correlation function into separate attractive (solid blue line) and repulsive (solid red line) components. The correlation terms from both parts can be directly added to reproduce the realistic two-point correlation function. This parameterization method has no isospin dependence and represents an average correlation effect.

Based on the results in Fig. 9, although the true two-point correlation function exhibits isospin dependence, the initial-state quantities of heavy-ion collisions fail to demonstrate isospin-dependent correlation properties when compared to the average two-point correlation function. It reflects that the current quantities are all influenced by the average isospin correlation effect. Consequently, as long as the correlation functions exhibit the same average effect, the final impact on the observables will also be identical. This arises from our initial-state modeling assumption of an isospin-independent nucleon-nucleon cross section. It also points to a possible new direction for improving phenomenological models for heavy-ion collisions.

It is noteworthy that the attractive and repulsive ef-

fects in the realistic two-point correlation function mutually cancel. In contrast, this is not the case for the correlation functions in the currently popular NLEFT and VMC models [10], as they have only a single central attractive or repulsive effect. Neither model well captures the abrupt change in the correlation function observed at ~ 1.0 fm.

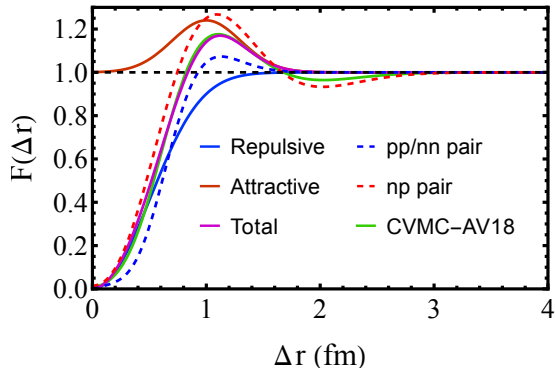


FIG. 8: The two-point correlation function for CVMC-AV18 interaction (solid green line) and its repulsive part (solid blue line) and attractive part (solid red line). The dashed red line and the dashed blue line represent the two-point correlation functions for the np pairs and the pp/nn pairs, respectively.

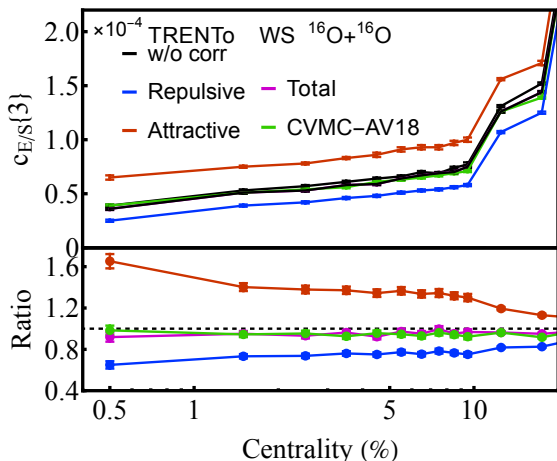


FIG. 9: The TRENTo results on $c_{E/S}\{3\}$ and its ratio $R(c_{E/S}\{3\})$ with isospin-dependent CVMC-AV18 interaction (solid green line), repulsive part (solid blue line), attractive part (solid red line) and the sum of two parts (solid purple line).

Appendix D: Analytical results of cluster structure

Figure 10 shows the analytical results on the dependences of ε_2 , ε_3 and the RMS radius on the parameters D_1 and D_2 based on the 4α -cluster structure of ^{16}O . The corresponding clustering geometry is illustrated in the inset of the left panel of Fig. 11. This panel also presents the effective one-body density $\rho_{cor}^{(1)}$ for four α -clusters inside ^{16}O . When $\gamma > 0$, the attractive correlation effect in the center causes a slight increase in central density, while the opposite effect occurs when $\gamma < 0$. For $\alpha = 3$, the ratio indicates a correlation effect of approximately 1%, while for $\alpha = 1$, the correlation effect is approximately 5%. We compare NN correlation effect on $c_{E/S}\{3\}$ in both the spherical nuclei and the clustering structures in the right panel of Fig. 11. The NN correlations primarily affect local energy density fluctuations in the initial state of HICs, with the result that the NN correlation effect in clustering structures is weaker than that in spherical nuclei for both cases,

$$\Delta R(c_{E/S}\{3\})_{WS} > \Delta R(c_{E/S}\{3\})_{Cluster}. \quad (D1)$$

This occurs because the clustering model intrinsically incorporates repulsion between clusters and strong binding within them, thereby suppressing the additional influence of NN correlations, regardless of the attractive or repulsive nature of NN correlations.

Appendix E: Probability distribution of $\langle E/S \rangle$

In Fig. 12, we use $\langle E/S \rangle$ to estimate the transverse system size for three correlation scenarios, i.e., a Woods-Saxon distribution without correlations (black), and with attractive (red) or repulsive (blue) leading-order correlations, respectively. In the bottom panel, the central values are aligned to compare distribution shapes directly, and the dashed curves show the corresponding Gaussian fits to guide the eye. All three distributions exhibit positive skewness. Relative to the uncorrelated case, an attractive correlation (solid red) slightly enhances this skewness, whereas a repulsive correlation (solid blue) moderately reduces it, consistent with the calculations in the main text. This provides an interpretation in terms of the $\langle E/S \rangle$ probability distribution for the behavior of the third-order cumulant in the transverse system size.

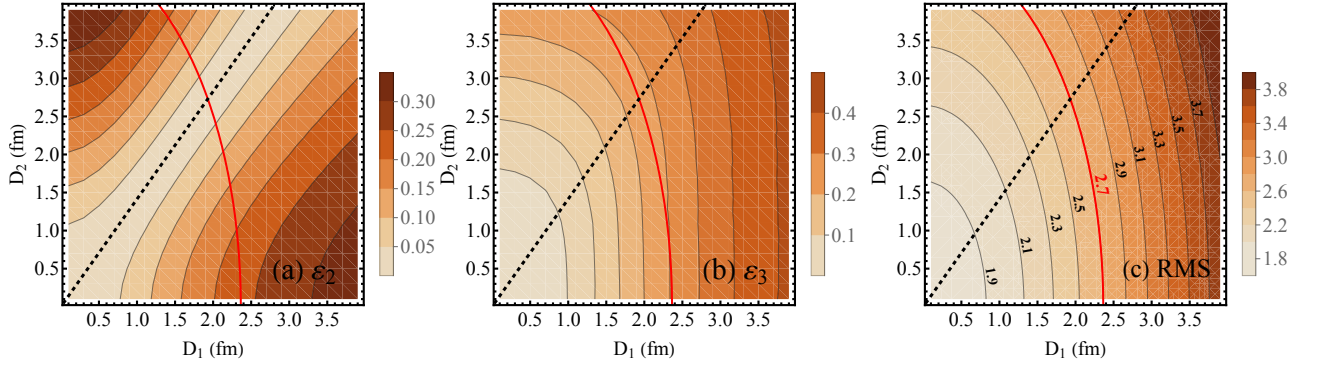


FIG. 10: The analytical results on the dependences of (a) ε_2 , (b) ε_3 and (c) RMS on the parameters D_1 and D_2 for tetrahedral ^{16}O . The solid red line represents a fit to the experimental RMS radius, while the black dashed line ($D_2/D_1 = \sqrt{2}$) indicates a regular tetrahedral structure.

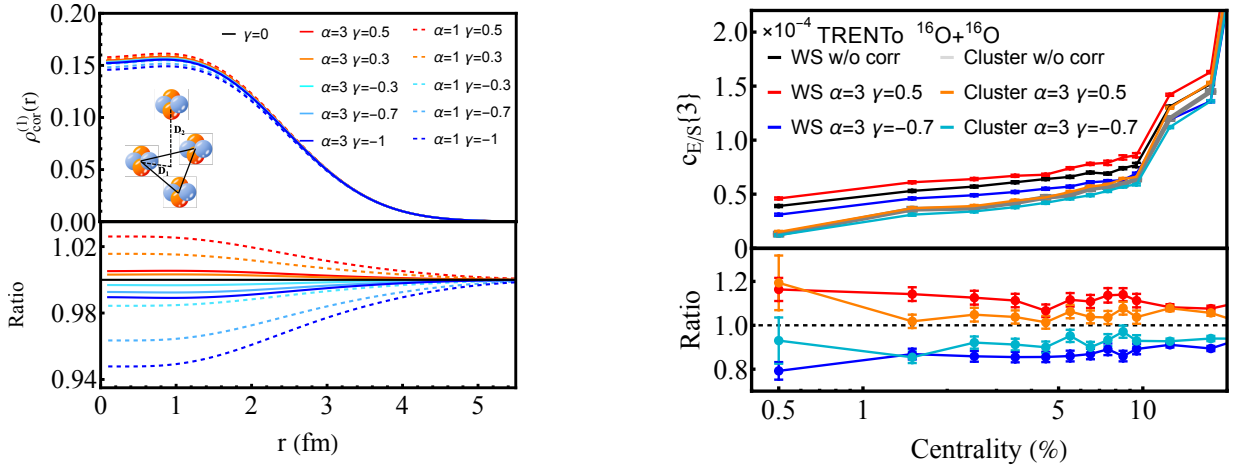


FIG. 11: Effective NN-correlated one-body density distributions $\rho_{cor}^{(1)}$ for four α -clustered ^{16}O with parameters $D_1 = 1.6$ fm and $D_2 = 3.5$ fm (left panel). The TRENTo results on $c_{E/S}\{3\}$ and its ratio $R(c_{E/S}\{3\})$ for WS distribution and clustering distribution under leading order attractive correlations and repulsive NN correlations (right panel).

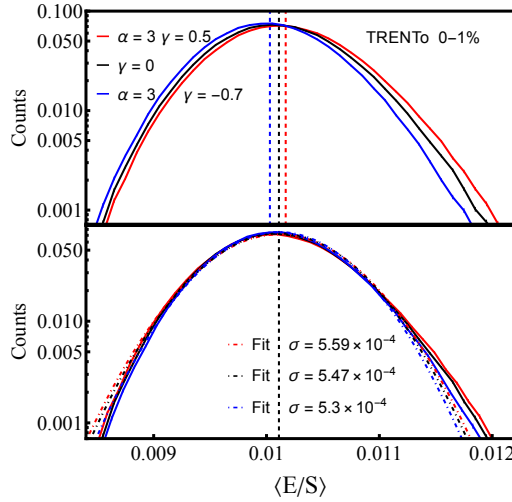


FIG. 12: Top panel: the TRENTo results on probability distribution of $\langle E/S \rangle$ in 0–1% central $^{16}\text{O}+^{16}\text{O}$ collisions with a Woods-Saxon distribution without NN correlations (black), and with attractive (red) or repulsive (blue) leading-order NN correlations. Bottom panel: The same three cases with their central values aligned for direct comparison of distribution shapes.